Lab on a Chip

PAPER

View Article Online
View Journal | View Issue

Cite this: *Lab Chip*, 2025, **25**, 5255

Topographic cues regulate collective cell dynamics in curved nano/microgrooved tubular microchannels

Tatsuya Matsubara, †[a] Chris P. Miller,†‡[b] Chanhong Min,[a] Chia-Yi Su,[acd] Jong Seob Choi,[ae] Chwee Teck Lim,[fg] Jude M. Phillip,[ahijkn] Joon-wan Kim[l] and Deok-Ho Kim *[ajkmn]

Received 16th April 2025,
Accepted 1st September 2025

DOI: 10.1039/d5lc00368g

rsc.li/loc

Physical properties of the extracellular matrix, such as topography and curvature, regulate collective epithelial behaviors. However, the interplay between these geometric factors on collective migration is not well understood. In this study, we investigate the effects of topographic cues on a curved surface on collective epithelial migration within tubular microchannels with an inner diameter of 100 μm. These tubular microchannels feature circumferential or longitudinal micro- and nano-grooves fabricated by two-photon polymerization three-dimensional printing and micro-molding techniques. Live cell microscopy records the collective migration of GFP-labeled epithelial cells into the microchannel with each topographical design. We utilized a single-cell behavior analysis for the tracked time-dependent cell position data to visualize and quantify complex cell migration. Results show that longitudinal grooves (800 nm and 4 μm) enhanced cell migration, but circumferential grooves did not significantly enhance cell migration. This indicates that curvature rather than topography dominates migration at the microtube scale. These findings provide insights into the interplay between curvature, microscale structure, and cell behaviors and suggest the potential to control cell behaviors by manipulating the structure and topographic cues with their local microenvironments.

[a] *Department of Biomedical Engineering, Johns Hopkins University, Baltimore, MD 21205, USA*
[b] *Translational Science and Therapeutics Division, Fred Hutchinson Cancer Center, Seattle, WA 98109, USA*
[c] *Institute of Biophotonics, National Yang Ming Chiao Tung University, 11221, Taiwan*
[d] *Bachelor Program in Digital Healthcare, National Yang Ming Chiao Tung University, 11221, Taiwan*
[e] *Division of Advanced Materials Engineering, Kongju National University, Cheonan, Chungnam, 31080, South Korea*
[f] *Department of Biomedical Engineering, National University of Singapore, Singapore 117583, Singapore*
[g] *Mechanobiology Institute, National University of Singapore, Singapore 117411, Singapore*
[h] *Department of Chemical and Biomolecular Engineering, Johns Hopkins University, Baltimore, MD 21218, USA*
[i] *Department of Oncology, Sidney Kimmel Comprehensive Cancer Center, Johns Hopkins School of Medicine, Baltimore, MD 21205, USA*
[j] *Institute for Nanobiotechnology, Johns Hopkins University, Baltimore, MD 21218, USA*
[k] *Translational Tissue Engineering Center, Johns Hopkins University, Baltimore, MD 21205, USA*
[l] *Laboratory for Future Interdisciplinary Research of Science and Technology (FIRST), Institute of Integrated Research (IIR), Institute of Science Tokyo, Yokohama, Kanagawa 226-8503, Japan*
[m] *Department of Medicine, Johns Hopkins University School of Medicine, Baltimore, MD 21205, USA. E-mail: dhkim@jhu.edu; Tel: +1 410 502 9773*
[n] *Center for Microphysiological Systems, Johns Hopkins University, Baltimore, MD 21205, USA*
† Contributed equally to this work.
‡ Co-first author.

Introduction

Collective cell migration is a critical process in various biological events,[1] including wound healing,[2] cancer metastasis,[3] and tissue formation.[4] Cells navigate by aligning along fibrous proteins in the extracellular matrix (ECM).[5,6] The ECM impacts cell migration and morphology through geometry, anisotropy, and stiffness.[7–10] To better understand these intricate mechanisms, engineered ECMs have been developed for *in vitro* experiments.[11] Research on engineered ECMs involves the fabrication of one-dimensional linear[12] and two-dimensional (2D) planar micro- and nanogrooves,[13–20,61] as well as micropillars,[21] using photolithography in micromechanical systems (MEMS). These studies have demonstrated that grooves are crucial in inducing morphological changes and promoting cell migration.[22] However, cell migration and morphology are affected not only by topography but also by curvature.[23,24] For instance, investigations using tubes with varying diameters have explored the influence of curvature (tube diameter) on cell migration and morphology.[25] Additional research has examined distorted microchannels[26] and microchannels with intricate cross-sectional shapes.[27] Engineering models have been developed for both the inner (concave) surfaces and the outer (convex) surfaces, such as cylinders,[28,29]

semicylinders,[30] and hemispheres.[31] Current studies utilizing computational modeling and theoretical models on curved surfaces, where both concave and convex features coexist, are also investigating the effects of curvature on cell morphology.[32–36]

While it has been established that both topography and curvature influence cells, the behavior of cells in complex environments, specifically within microchannels featuring curved scaffolds with micro- and nanostructures on the inner surface, has yet to be comprehensively explored. Our bodies contain a variety of hollow microchannels embedded within the ECM, making it essential to study curvature and topography *in vitro*. Examples of replicating both factors involve applying a thin film of fibrillar collagen network[37,38] or electrospun microfiber[39] onto structures such as semi-cylinders and hemispheres. One previous study[37] investigated alterations in cell migration and orientation due to variations in diameter ranging from 250 μm to 5 mm. However, exploring cell migration in microchannels with precise topography remains largely uncharted. Furthermore, most such studies primarily evaluated cell morphology, with limited insights into cell migration.

Precisely fabricating microstructures on the inner surface of 3D microchannels remains challenging.[40] First, conventional fabrication techniques, including photolithography in MEMS, can fabricate precise microstructures[59,60,62,63] but have difficulty processing 3D shapes. Methods that involve rolling thin film sheets with micropatterns created using photolithography[41,42] may be challenging for handling microchannels with small diameters. Next, while electrospinning methods[39] for fiber formation can create 3D fibers with controllable diameters, the precise control of fiber orientation and spacing is intrinsically difficult. Techniques based on the phase separation phenomena of immiscible polymer blends can generate unique topographies, but achieving uniform groove shapes and dimensions is challenging.[43] Focused ion beam microfabrication allows for precise 3D processing of high-strength molds, including metals. Still, it is limited to only the processing region unless a system for automatically rotating the sample is installed. Therefore, we focused on the two-photon polymerization (2PP) 3D printing method.[44] Among various 3D printing techniques,[45] this technology involves initiating cross-linking reactions in UV-curable resin where two photons arrive simultaneously, forming complex 3D shapes one layer at a time. The disadvantage of 2PP's long fabrication times can be resolved, enabling reusable mold formation with exceptionally high precision.[46] Using the 2PP method, microstructured environments have been created to quantitatively assess geometry-dependent YAP and MRTFA signaling in neuronal cells.[47] However, how cells respond to such fine structures within confined tubular microchannels remains poorly understood.

This study introduces a 3D tubular structure with micro- and nanogrooves on the inner surface (Fig. 1A). Using a high-precision 2PP 3D printing technique, we fabricated a pair of semi-cylindrical molds (100 μm in diameter) for the tubular microchannel with the micro- and nanogrooves on the inner

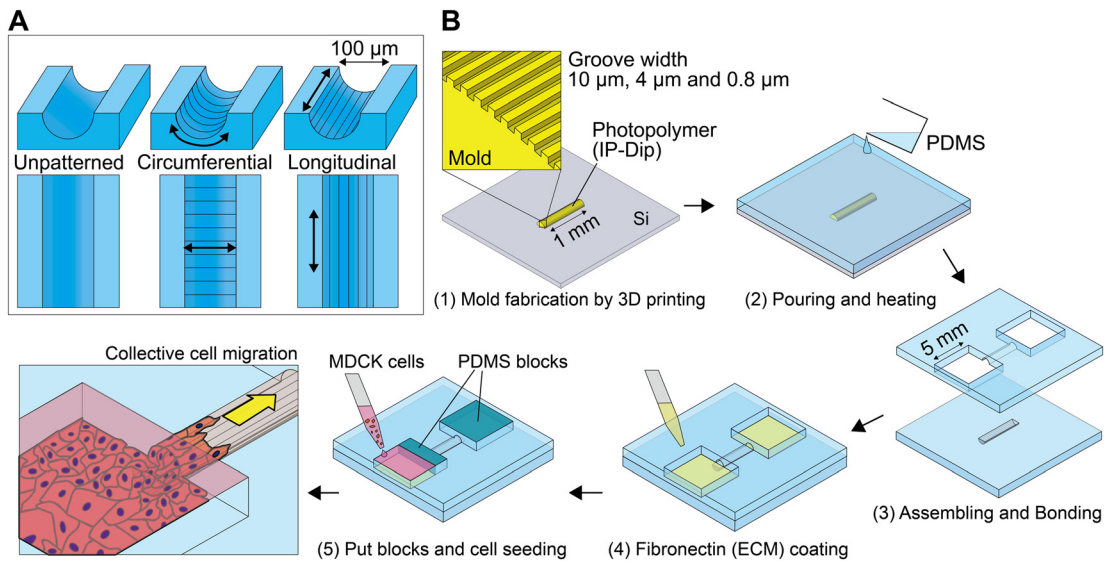

Fig. 1 Fabrication of tubular microchannels with interior micro- and nanopatterning and seeding of epithelial cells. (A) Schematic illustration of the patterning designs. The groove widths are 10 μm, 4 μm, or 800 nm. (B) Fabrication process and cell seeding workflow. (B-1) The semi-cylindrical mold is fabricated by a laser direct drawing machine onto a silicon wafer. After UV exposure, the unexposed area is removed by the developer PGMEA. The length of the printed mold is 1 mm with 100 μm in diameter. (B-2) PDMS is poured onto the molds after baking. (B-3) An upper PDMS part is prepared, cut, and fitted to the bottom PDMS part. (B-4) To enhance the adhesion of cells with the PDMS surface, fibronectin (50 μg ml^{-1}) (indicated by yellow) is applied for one hour. (B-5) After washing with PBS, cells (1000 cells per mm^2) are seeded onto one side of the chamber (5 mm × 5 mm). The entrance area and the other side of the chamber are blocked with a PDMS block (indicated by green) to prohibit cell invasion. After one day, the PDMS block is removed from the chamber when the cells have reached confluence to initiate cell migration.

surface. We observed the collective migration and morphology of epithelial cells in such microtubes to assess the impact of these micro- and nanogrooves. Through this investigation, we experimentally verified the influence of topography and curved surfaces on cell migration and morphology.

Materials and methods

Design and fabrication of micro/nanopatterned tubular microchannels

In this study, we prepared a tubular microchannel through a five-step process involving mold formation, molding by polydimethylsiloxane (PDMS), assembly of the respective components, protein coating, and cell seeding (Fig. 1B). The mold was first fabricated in a 3D high-resolution printer (Photonic Professional GT2, Nanoscribe GmbH & Co. KG), creating a semi-cylindrical shape with micro- and nanogrooves on the inner surface of the tubular microchannel. These grooves had widths of 10 μm, 4 μm, and 800 nm in the circumferential and longitudinal directions. A 2PP 3D printing obtained a highly accurate pattern using the photosensitive resin IP-Dip (Nanoscribe GmbH & Co. KG) and UV exposure. The structures were fabricated using a 63× oil-immersion objective lens in fulfill mode with a laser power of 60 mW and an exposure time of 200 ms. Slicing and hatching distances were set to 0.3 μm and 0.1 μm, respectively. The printing was performed in Galvo scan mode with one-way hatching, using a voxel aspect ratio of 1.0 and a piezo-driven *Z*-stage. The unexposed portions were then removed with the developing solution propylene glycol monomethyl ether acetate (PGMEA) for 10 minutes and cured by heating at 65 °C for 10 minutes.

Next, the molding process for PDMS (Sylgard184, Dow Corning Toray) started with placing the taped mold in a plastic case. Degassed PDMS with a mixing ratio of 1 : 10 was poured into the mold, and the amount was adjusted to ensure the thickness of the part was less than 500 μm since a thicker part may compromise the resolution during recording. The PDMS was vacuumed for 30 minutes and then placed in an oven at 65 °C for 2 hours, allowing it to cross-link. After carefully peeling off the PDMS from the Si chip, a pair of molded PDMS chips were assembled into the upper and lower semi-cylindrical components. Excess portions were trimmed as needed. To complete the process, a square-shaped chamber for cell culture was created at the inlet and outlet of the upper tube part by cutting the PDMS block accordingly.

In the final step of the tubular microchannel assembly process, the attaching surfaces of the two PDMS microchannels underwent treatment with O_2 plasma at 100 cm^3 min^{-1}, 100 W, for one minute. The surfaces were carefully aligned manually with the aid of a methanol droplet and bonded within 2 minutes. Subsequently, the assembled PDMS was placed in an oven at 65 °C for 10 minutes. Following this, the bottom of the assembled PDMS microchannel received a second O_2 plasma treatment to facilitate bonding to the glass surface of a single bottomless well. Again, the device was placed in a 65 °C oven for 10 minutes.

Cell culture

Within one minute of treating the sterilized PDMS microchannel with O_2 plasma, a 50 μg mL^{-1} fibronectin solution (100 μL) was introduced into a chamber at the microchannel entrance and flowed to the opposite chamber. Then, we dispensed 2 mL of fibronectin solution throughout the single well and incubated it at 37 °C for an hour, reducing the risk of incomplete coating due to residual air within the microchannel. After aspirating the solution and rinsing with 2 mL PBS, 100 μL of Dulbecco's modified Eagle's medium (GIBCO, USA) was added to the entrance chamber for cell seeding with 100 μL of medium added to the exit chamber one minute later. All culture media included 10% fetal bovine serum (Thermo Fisher Scientific, USA) and 1% penicillin–streptomycin (10 000 units per mL) (Thermo Fisher Scientific, USA).

Before seeding cells, a pre-cut rectangular PDMS block (25 mm^2) was positioned in the chamber on the outlet side. A portion of another PDMS block was placed at the entrance, allowing cell culture to be introduced exclusively on the entrance side without entering the microchannel. To prevent cell ingress into the outlet side, 20 μL of the medium was applied over the PDMS block, maintaining high back pressure. We seeded 10 μL of H1-GFP-transfected Madin–Darby canine kidney (H1-GFP-MDCK) cells (1.0×10^5 cells per cm^2, 2.5×10^6 cells per mL) into the entrance chamber (cells kindly provided by Prof. Chwee Teck Lim, National University of Singapore). Microscopic observation confirmed that no cells had entered the tubular microchannel. If cells flowed into the tubular section from the seeding areas, the pressure difference was counterbalanced by adding medium to the exit side PDMS block. We incubated the cells at 37 °C in a humidified atmosphere with 5% CO_2.

After the cells had adhered to the bottom (approximately 2 hours), 3 mL of medium was added to the entire single well. When cell confluence reached 80–90% (after 2 days), we removed the PDMS blocks from the chambers, and the medium was aspirated from the well and chamber. Then, 100 μL of the medium was introduced to the outlet chamber side, opposite the cell-seeded chamber, to eliminate particles inside the tubular microchannels. Finally, 2 mL of fresh medium was replenished into the well.

Time-lapse live cell imaging

When the entrance PDMS block has a thickness of 0.5 mm, cells reach the entrance area about one day after the block's removal, giving a cell migration speed of approximately 0.4 μm min^{-1}. After cells arrived at the entrance, we replaced the culture medium. We secured the microchannel device to the live-cell confocal microscope by using a spinning disk unit

(W1, Yokogawa). We set the 488 nm laser intensity to 1% and performed time-lapse imaging at 10-minute intervals for up to 12 hours using multi-position settings in a 37 °C 5% CO_2-humidified atmosphere. We captured *z*-stack images with a 10× lens, ensuring a 0.9 μm thickness to include the entire tube cross-section.

Quantitative cell image analysis

Time-lapse 3D live cell imaging was analyzed using Imaris software. Individual cells were tracked as particles for position and time frame information. Particles progressed through time frames set at 10 minute intervals. A cell's migration parameter was represented by its average migration velocity, calculated from its trajectory. Cells with five or fewer tracks were removed from the calculations. The heat map divided the microchannel into 20 μm intervals along its axis. The average cell migration velocity was computed for regions containing a minimum of three cells.

Trajectory registration

To standardize trajectory analysis and minimize the influence of length and direction, we adjusted all trajectories to a uniform duration of 3 hours. Only trajectories with continuous tracking for at least 3 hours were retained to ensure data quality. To enhance tracking accuracy, any trajectory with missing frames was excluded. At each time point, consecutive centroid positions were recorded, allowing for the quantification of various migration features using a custom-built feature extraction pipeline.

Migration feature extraction

To characterize single-cell movement, we extracted 93 migration features encompassing a broad range of movement dynamics.[48,49] These features include displacement-based and turning angle-based metrics, capturing aspects such as magnitude, distribution patterns, signal properties, temporal correlations, entropy, and decomposed components. All migration features are listed in Table S1.

Outlier detection

To detect the noisy outliers, the entire migration space was visualized with UMAP to identify 'small islands' that are distinguishably away from the 'mainland' consisting of majority of data points. We classified the small island outliers by sorting the data each in UMAP1 and UMAP2 direction and detected sudden largest difference in the consecutive UMAP1 or UMAP2 values. Therefore, any disconnected small subsets are marked as outliers.

Dimensionality reduction and unsupervised clustering

To analyze multidimensional migration features, we applied principal component analysis (PCA) to eliminate parameter covariances and retained principal components (PCs) accounting for 95% of the cumulative variance. These PCs were then used to generate two-dimensional projections *via* UMAP. For clustering, we employed the K-means++ algorithm to identify eight migration clusters (MCs). To validate these clusters, we visualized trajectory projections from each MC to assess qualitative similarities.[50] Additionally, Shannon entropy S was computed to quantify migration state heterogeneity with following formula.

$$S = \sum_{i=1}^{9} -p_i \cdot \log(p_i)$$

Here p_i is the fraction of cells within each migration cluster i.

Statistics and reproducibility

For statistical comparisons across multiple groups in Fig. 3, we applied the Kruskal–Wallis test followed by Dunn's *post hoc* analysis. Where necessary, data were scaled to normalize distributions for Gaussian-based models. All collected data were included in the analysis without exclusion. All analyses were performed in Python with the following software specifications: python 3.9.13, scipy 1.13.1, scikit-learn 1.1.13, scikit-image 0.19.3, scikit-posthocs 0.9.0, statsmodels 0.13.5, pandas 1.5.2, matplotlib 3.6.2, seaborn 0.11.2, umap-learn 0.5.3, and numpy 1.23.5, cmcrameri 1.9, EntropyHub 0.2, pyarrow 12.0.1.

Actin staining

Following a 12-hour migration period, MDCK cells underwent fixation with 4% paraformaldehyde (Thermo Fisher Scientific, USA), permeabilization using 0.1% Triton X-100, and then incubation with 594 Phalloidin (Thermo Fisher Scientific, USA) for one hour. Images were captured with a spinning disk confocal microscope utilizing a 20× lens in large image mode.

Cell morphology analysis

To quantitatively assess cell morphology, the 3D images of the stained cells within the tubular microchannel were initially unwrapped into 2D. The virtual unwrapping of the tubular microchannel was conducted using ImageJ (National Institutes of Health, USA) after background subtraction. Initially, the *z*-stacks of the tubes were resliced to obtain the *xz* plane. Next, a circle was fitted to the circumference of the tubular microchannel, converted to a line, straightened, and resliced again to create an image of the virtually unwrapped tube, with the tube circumference (*x*-axis) and tube length (*y*-axis). This process was coded in ImageJ to simplify converting a 3D timelapse image into 2D, facilitating the analysis while preserving the relevant *x*, *y*, and *z* information. In the flattened image, each cell's perimeter was manually traced, and the orientation and aspect ratio of the area was calculated using ImageJ.

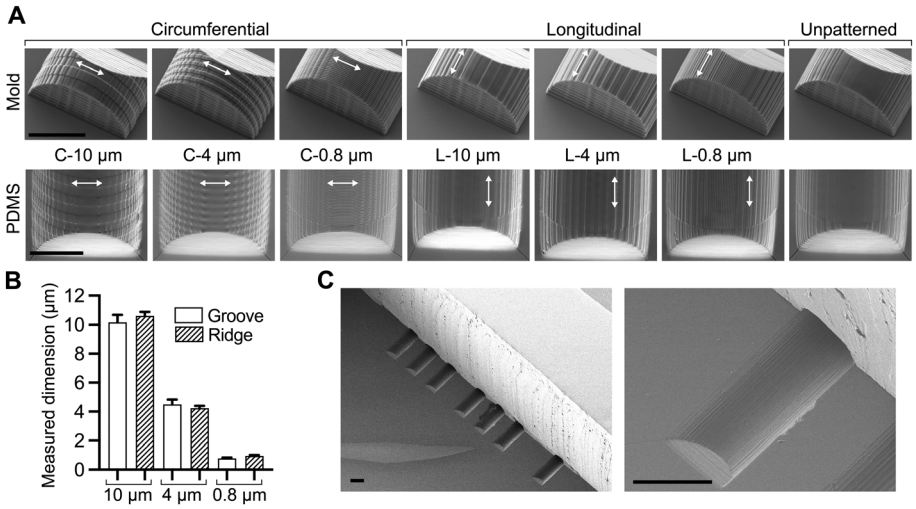

Fig. 2 Fabrication results of molds and molded PDMS microchannels with micro- and nanogrooves. (A) Representative scanning electron microscope images of semi-cylindrical printed molds and molded PDMS microchannels. The dimensions are designed as 10 μm, 4 μm, or 800 nm with circumferential, longitudinal, or unpatterned directions. Scale bars, 50 μm. (B) The measured width of micro- and nanogrooves from scanning electron microscope images using the image analysis software ImageJ. (C) Representative images of the assembled PDMS microchannels. Scale bars, 100 μm.

Statistical analysis

Data were analyzed using GraphPad Prism 9 (GraphPad Software, USA). One-way ANOVA was employed to compare statistical differences among various groups. Differences were deemed significant in all statistical analyses when $p < 0.05$.

Results

3D printing for the semi-cylindrical mold with precise micro- and nanogrooves

Fig. 2A presents typical scanning electron microscope images of the printed mold and the successfully transferred precise structures to the PDMS. Iterative experimentation produced a mold featuring a semi-cylindrical structure (diameter 100 μm) with the desired dimensions. The mold's surface was detached easily without requiring a special surface coating. Fig. 2B displays the measured groove and ridge widths in the mold, which are printed with high precision: (1) groove width 10.2 μm, ridge width 10.6 μm, (2) groove width 4.5 μm, ridge width 4.2 μm, and (3) groove width 0.8 μm, ridge width 0.9 μm. Due to the layer-by-layer printing principle, stacking marks between layers are observable in each mold. Although these may function as longitudinal grooves, we deem the effect acceptable, as the influence of layer stacking works as offset for all molds. Fig. 2C depicts an SEM image of the precisely aligned assembled PDMS flow microchannel, consisting of upper and lower flow microchannel parts. This PDMS chip comprises seven parallel tubular microchannels (three circumferential groove types, three longitudinal groove types, and one unpatterned). This parallel arrangement aims to provide a stable environment using the same cell culture batch while enabling live cell imaging observations of cell migration along the same time axis for each groove.

Differential single-cell migration behaviors of collective cell migration

To evaluate the influence of groove width and direction on cell migration speed, we recorded the 3D movement of cells using live cell imaging. Fig. 3A illustrates the migration of cells over time within the tubes featuring the designed grooves. Moreover, visualization software accurately tracked each cell as a particle (Fig. 3A bottom). By the tracked position of single cells in each time frame, we identified eight distinct migration clusters (MCs) based on an unsupervised *k*-means clustering ordering from MC0 to MC7 with increasing speed (Fig. 3B). The projected migration features of cells to UMAP space in Fig. 3C shows the relationship of representative migration features. For example, the high velocity group such as MC7 has low displacement coefficient of variance (CV) and average turning angle (TA). Since the value of Disp. CV and TA indicates the relative variability of cell's movement magnitude over time and tortuosity, the cells in MC7 group exhibit fast and highly progressive migration. Also, the representative trajectory of cells in MC7 (Fig. 3D) also support this relationship in Fig. 3C. The 2D UMAP kernel density estimation (KDE) represents multidimensional single-cell migration for each designed topography to visualize the similarity of the cell migration in each design (Fig. 3E). This shows that in the circumferential set the KDE peak stays in the same UMAP position but spreads wider as the grooves become larger, while in the longitudinal set the 10 μm pattern forms a compact low-UMAP2 cluster and the 4 μm and 0.8 μm patterns extend upward, anticipating the cluster shifts reported in Fig. 3F and G. Fig. 3F indicates that MC distribution of C0.8 and L10 is unpatterned-like, as described by the abundance of cells in the slowest cluster MC0. On the

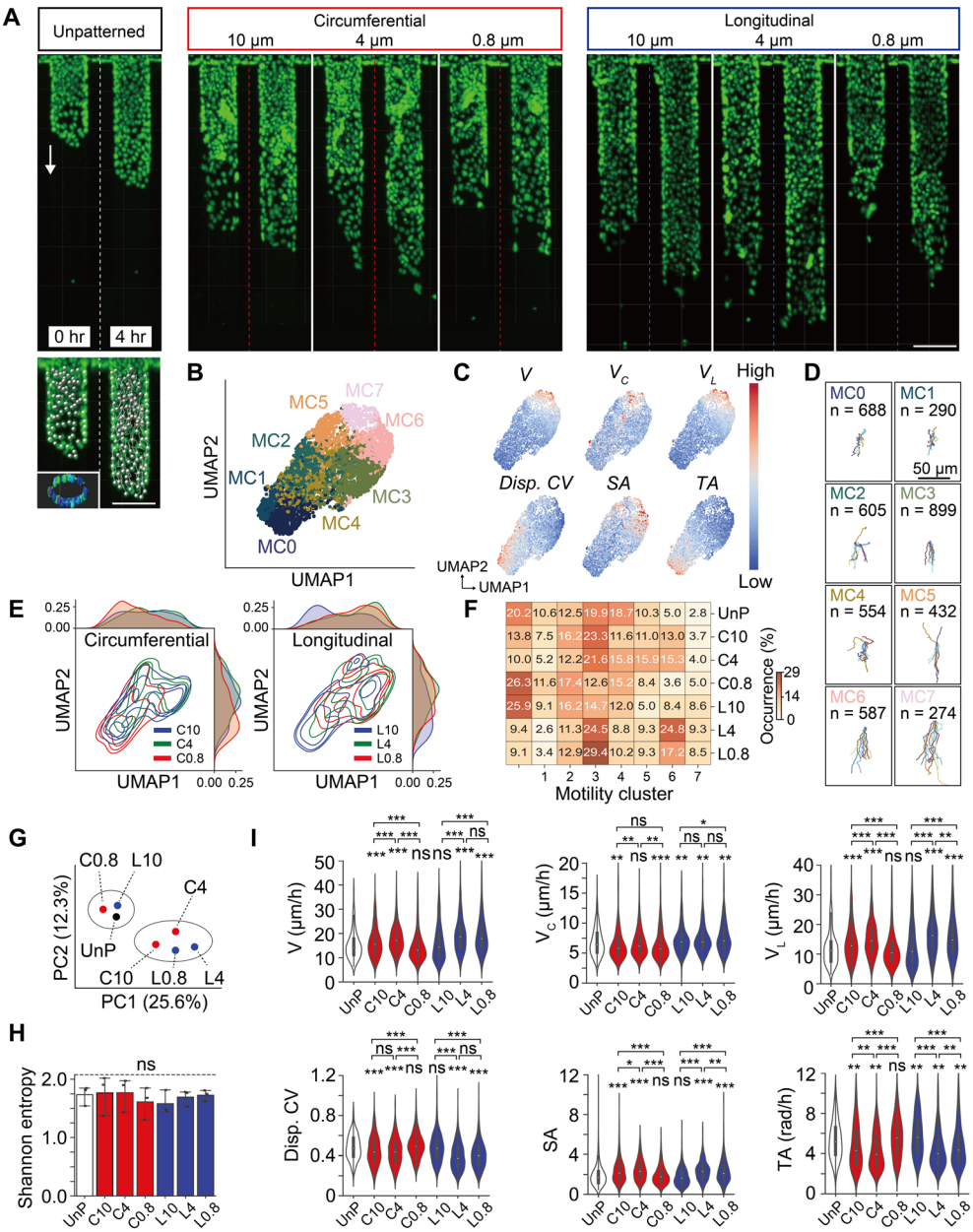

Fig. 3 Differential single-cell migration behaviors of collective cell migration in tubular microchannels with each designed topography. (A) Representative time-lapse images showing the collective migration of H1-GFP-MDCK cells within tubular microchannels (100 μm diameter), presented as top-view 2D projections of 3D *z*-stacks analyzed with Imaris 3D visualization software. Scale bars, 100 μm. (B) UMAP representation of unsupervised *k*-means clustering identifies eight unique migration clusters (MC). (C) *V* (average speed), V_C (average speed in the circumferential direction), V_L (average speed in the longitudinal direction), Disp. CV (displacement coefficient of variance), SA (spatial anisotropy), and average turning angle (TA) migration features projected onto the UMAP space. (D) Ten example movement trajectories are shown for each MC, and the corresponding total number of trajectories per cluster is annotated. Each trajectory is 3 hours long. (E) 2D UMAP kernel density estimation (KDE) representation of multidimensional single-cell migration for each topography (10 μm, 4 μm and 0.8 μm) of circumferential (left) and longitudinal (right) direction. 1D KDE across UMAP1 (top) and UMAP2 (right). (F) Heatmap of fraction occurrence of eight MCs across structure groove widths. Hierarchical clustering is based on the Euclidean distance using the Ward method. (G) Average principal components (PCs) computed from high-dimensional migration features per groove widths. Black circle indicates grouping of similar conditions in the PC space. Number in the parenthesis indicates variance captured by each PC. (H) Comparison of Shannon entropy computed for each experiments based on Kruskal–Wallis test followed by Dunn's *post hoc* test (n = 3 in each design). (I) Migration features were computed for each cell across structure groove widths based on Kruskal–Wallis test followed by Dunn's *post hoc* test for *V*, V_C, V_L, Disp. CV, SA, and average TA. *$p < 0.05$, **$p < 0.01$, ***$p < 0.001$, ****$p <$ 0.0001, ns is non-significant statistics that fail to reject the null hypothesis of the Kruskal–Wallis test. Comparison is done on control (unpatterned) *vs.* each topographical condition. Sample size for (G, I), n = 321 in UnP, n = 605 in C0.8, n = 829 in C4, n = 493 in C10, n = 528 in L0.8, n = 831 in L4, and n = 722 in L10. "n" in each cluster represents the total number of trajectories obtained from three independent experiments.

other hand, C4, C10, L0.8, and L4 were less abundant in MC0 and more dominant in faster MCs. Fig. 3G by average principal components (PCs) computed from high-dimensional migration features in each design visualized the similarity of C0.8, L10 and unpatterned, suggesting that in the circumferential condition, large groove size is required for the cells to sense the groove structure, whereas in the longitudinal, large groove size is not sensed by cells. Shannon entropy analysis showed no significant differences among the topographic conditions (Fig. 3H), suggesting that heterogeneity of MC distribution was comparable across groups. Based on this, we next quantified migration features related to movement magnitude and directionality under each condition (Fig. 3I).

The top graph of Fig. 3I, which shows the cell migration speed, reveals that channels with microstructures generally exhibit higher cell speeds than the unpatterned except C0.8 and L10. Cells in C10, C4, L4 and L0.8 are more active than the other conditions, consistent with the previously mentioned results in Fig. 3G. To evaluate cell movement in more detail for each direction, we compared the velocity (Fig. 3I, the two graphs on the top right). V_C represents the velocity in the circumferential direction of the microchannel, and V_L represents the velocity in the longitudinal direction of the microchannel. Due to the fluorescence stretching and drift in the *z*-axis, it is difficult to evaluate the movement in the *z*-axis direction. First, there is a significant difference in the design for V_C. Interestingly, cells on circumferential grooves showed reduced velocity in V_C compared to those on unpatterned or longitudinal surfaces. This may reflect a spatial limitation unique to the circumferential axis, where movement often involves out-of-plane components along the *z*-axis. Since such vertical displacements were not captured in our analysis, interpretation of V_C in this context remains inconclusive. Regarding V_L, C0.8 and L10 show no significant difference, while C10 and C4 exhibit a higher migration speed. This result for circumferential grooves differ from previous studies, which showed that cell sheet leading edges exhibit lower migration speeds on flat substrates with topography perpendicular to the direction of movement.[51] Our results suggest that the curved shape has a more significant effect on assisting cell movement to the axial direction than the restraining effect by the circumferential grooves. L4 and L0.8 increase the migration speed as we expected. The wider groove (L10) is not affected. These results imply that the dimensions of microstructures, their directionality, and the cell sheet region are essential factors in curved surfaces.

The graph in the bottom of Fig. 3I, which shows the Disp. CV (displacement coefficient of variance), SA (spatial anisotropy), and average turning angle (TA), which respectively represent the variability in displacement, the degree of directional bias calculated by the ratio of displacement in the longitudinal over the circumferential direction, and the extent of turning behavior during migration. Conditions such as C0.8 and L10 show trends comparable to unpatterned, whereas other groups (C10, C4, L4, and L0.8) indicate significantly different characteristics. Specifically, C0.8 and L10 show lower Disp. CV, higher SA, and lower TA, indicating steady pace, more anisotropic towards longitudinal direction, and more directionally persistent migration. While groove size and orientation do influence migration, their overall effect seems limited in magnitude.

Effect of micro- and nanopatterning in the cell sheet leading edge and the trailing region

The tracked trajectories at the single-cell level and their instantaneous speed at each time point are shown in Fig. 4A. These results suggest that the longitudinal groove tubes have a lower cell density at the cell sheet leading edge than other grooves and that the speed at the cell sheet leading edge in all designs is higher than in the trailing cell region. We compared the cell density ratio at the cell sheet leading edge (200 μm from the edge) and the trailing region (200 μm from the microchannel entrance) of the migrating cells (Fig. 4C). For each groove, the density ratios are all less than or equal to 1, indicating active cell migration at the cell sheet leading edge. While the unpatterned and circumferential groove groups exhibit similar ratios, the longitudinal groove group shows no significant differences depending on groove width but consistently has smaller ratios. These findings suggest that longitudinal grooves substantially contribute to cell migration at the cell sheet leading edge.

Fig. 4B presents a heatmap to investigate the temporal and spatial changes in speed, with the results for the circumferential and longitudinal dimensions. Significant differences exist between the circumferential and longitudinal directions. While the circumferential grooves exhibit apparent speed differences between the cell sheet leading edge and trailing regions, the longitudinal grooves show smaller differences in speed between these regions. To quantitatively visualize this trend, we calculated the average speed across time frames and plotted the distance from the cell sheet leading edge against the speed (Fig. 4D). The visualization results reveal that while the longitudinal grooves maintain speed in the trailing regions, the circumferential grooves and unpatterned decrease speed in these areas.

Next, we considered why the longitudinal grooves can maintain speed in the trailing regions. We focused on a parameter called the straightness of each cell. This parameter is calculated from the velocity field of cells tracked as individual particles in the software. It is the ratio of the distance between the cell's starting and ending points (shortest distance) to the traveled distance. A ratio of 1 means that the cell travels the shortest distance. The results in Fig. 4E indicate that cells in the longitudinal grooves exhibit high straightness, while cells in the circumferential grooves show low straightness or similar straightness to the unpatterned. Moreover, the 800 nm longitudinal grooves, which likely function as topography, promote active cell

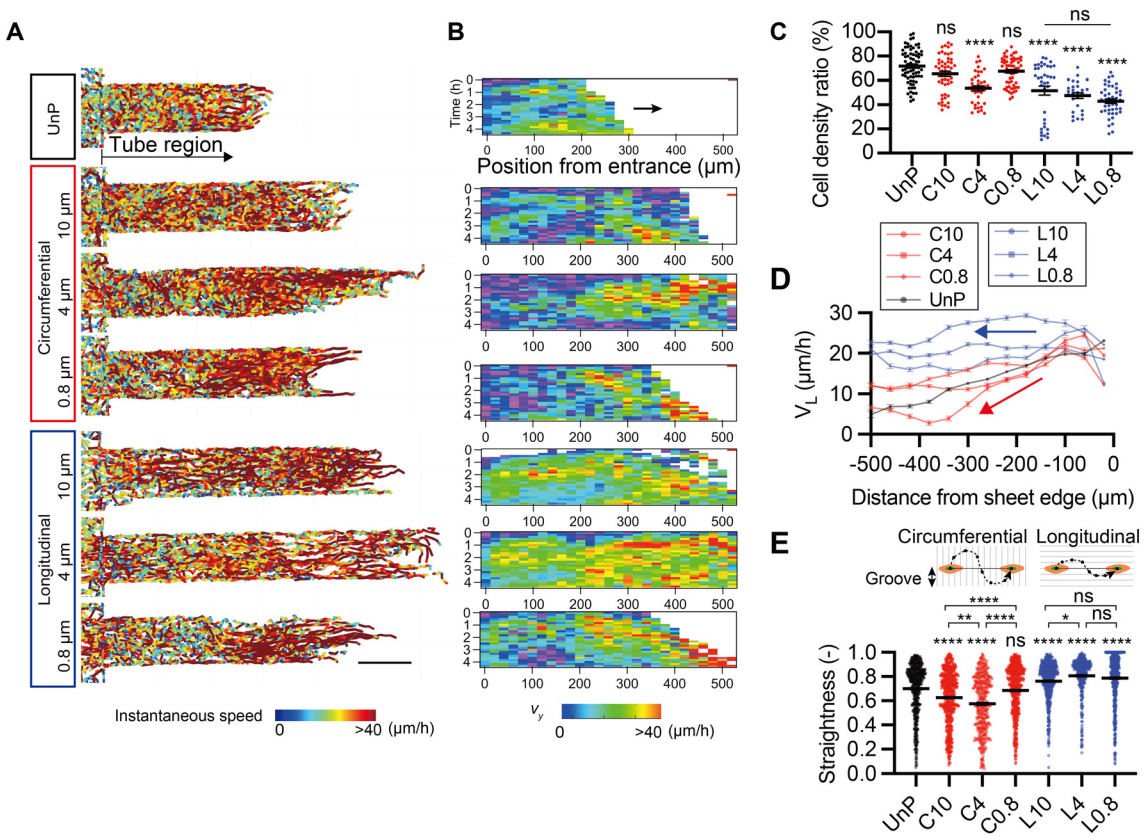

Fig. 4 Migration velocity difference at the cell sheet leading edge and trailing region in each topography design. (A) Representative cell tracking images showing the trajectory of cell migration after 4 hours in a microchannel with each topography. The trajectory color indicates instantaneous speed at 10 minute intervals of 4 hours. Scale bars, 100 μm. (B) Average velocity heat maps of 4-hour migration of H1-GFP-MDCK cells on different topographies in steps of 10 min. (C) The cell density ratio in each design in the cell sheet leading edge region (sheet edge to 100 μm) *versus* the trailing region (tube entrance to 100 μm) is plotted for each design. The longitudinal group shows a lower density ratio. The black bar represents the mean ± SEM of the cell density ratio in 25 frames. The *p*-values on the plots for each condition are compared to the unpatterned data. (D) *Y*-axis velocity with the distance from the cell sheet leading edge. Zero on the *x*-axis means the position of the cell sheet leading edge. The arrows indicate the trend of velocity change in the longitudinal group and the circumferential group. Data represent mean ± SEM calculated from 25 frames in the step of 10 min. (E) Straightness of the moving cells in each design. The upper schematic is an image of the cellular movement affected by grooves in different directions. Bar represents each mean of at least 4 hours (>25 frames). ns non-significant, $*p < 0.05$, $**p < 0.01$, $***p < 0.001$, $****p < 0.0001$ by one-way ANOVA.

migration at the cell sheet leading edge with a similar level of straightness as the 4 μm grooves.

Nevertheless, the heatmap visualization shows that the effect of the 800 nm longitudinal grooves diminishes in the trailing regions, unlike the 4 μm and 10 μm grooves. As expected, due to the more significant cell–cell contact in the trailing regions, the effect of the grooves at the topography order is relatively diminished, further supporting this assumption.

Cell orientation and elongation

To evaluate the morphology of the cells, we stained F-actin inside the tubes after the cells finished migration and imaged them using a spinning disk confocal microscope. Images of the cell nuclei and actin, as well as the upper and lower surfaces, are shown in Fig. 5A. Images of the circumferential and longitudinal grooves represent the 800 nm width results. Interestingly, for the unpatterned condition, there are apparent differences between the upper and lower surfaces. Looking at the fluorescent images of the cell nuclei, cells on the upper surface showed oriented alignment in the longitudinal direction. In contrast, the lower surface exhibited alignment in the circumferential direction.

Similarly, F-actin staining revealed that the cells are extended in the longitudinal direction on the upper surface, while this is not the case on the lower surface. A study using tube structures without microstructures (unpatterned)[25] reported that cells align in the longitudinal direction in smaller tubes (less than 100 μm), consistent with our results on the upper surface. If curvature were to function as the dominant factor in providing mechanical guidance to the cells, we would expect the same effects on both the upper and lower surfaces. The differences between the upper and lower surfaces are unlikely due to the cells' weight because the downward force caused by their weight would reduce the effect of topography on the upper surface and make the lower

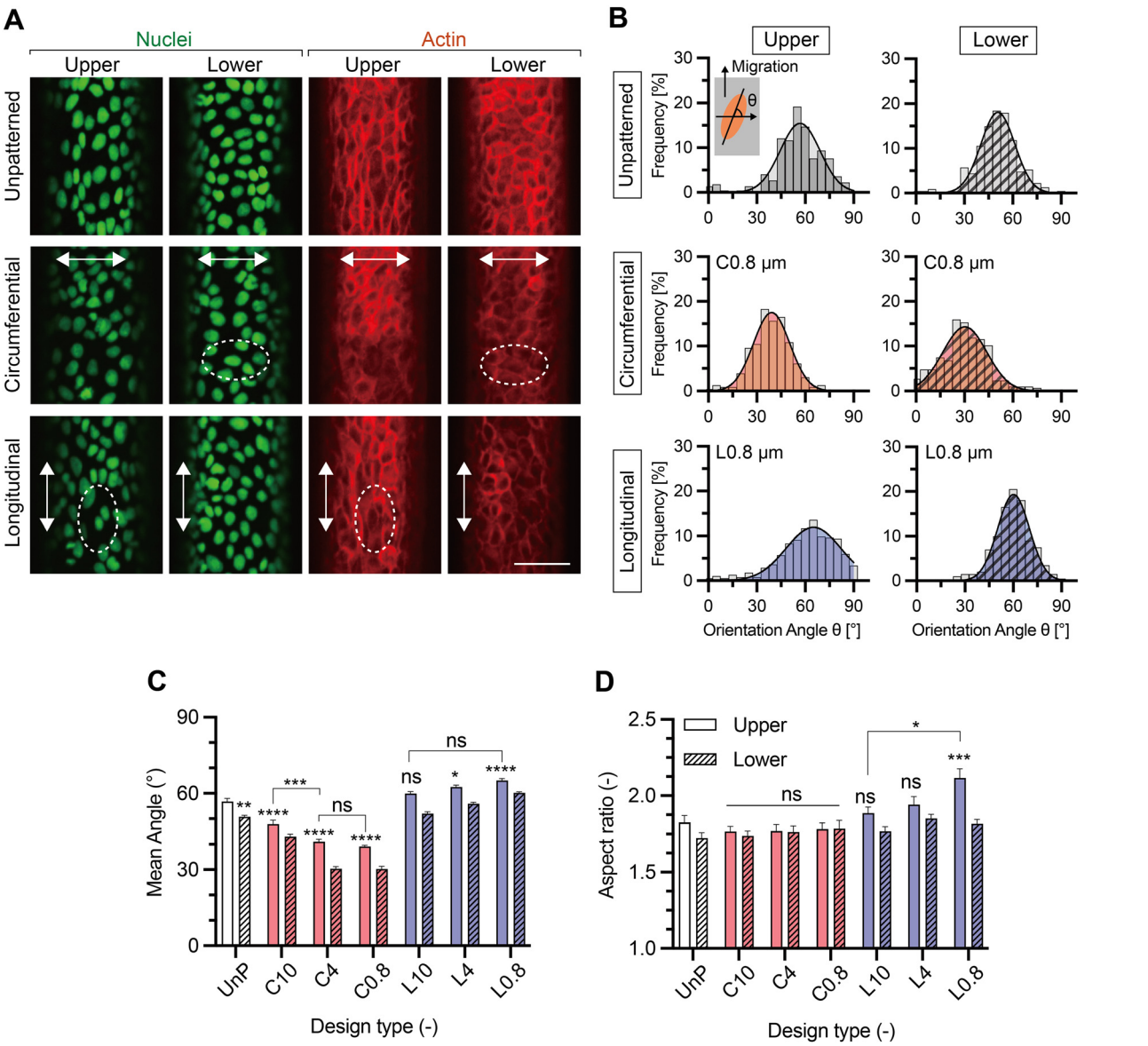

Fig. 5 Morphological cell analysis in different topography. (A) Representative fluorescent images of upper and lower curved surfaces in *z*-stack images showing groups of migrating MDCK cells inside the microchannel. Nuclei are shown in green by H1-GFP, and cells were stained for actin (phalloidin, red). Scale bars, 50 μm. (B) Cell angle distribution of nuclei and actin in upper and lower curved surfaces. The angle of cells is calculated from the cell orientation to the *x*-axis in absolute value. 90 degrees means orientating the cell to the *y*-axis. Both 70 degrees and 110 degrees are counted as 70 degrees. (C) The mean angle is calculated from the cell angle distribution of actin. The asterisk above the bar represents the test result compared to the upper unpatterned by one-way ANOVA. (D) Mean of the aspect ratio of elongated cells. ns non-significant, $*p < 0.05$, $**p < 0.01$, $***p < 0.001$, $****p < 0.0001$ by one-way ANOVA.

surface more susceptible to the influence of the tube's surface characteristics. The reasons for these differences between the upper and lower surfaces will be elucidated in future research.

Taken as a whole, we conclude that micro- and nanogrooves can influence cell alignment. Longitudinal grooves align cells in the longitudinal direction. In contrast, circumferential grooves orient cells in the circumferential direction. To quantitatively assess cell morphology, we quantified the orientation angle of actin-stained cells in Fig. 5B. The longitudinal (circumferential) direction is defined as 90 degrees (0 degrees), respectively. For unpatterned samples, upper cells predominantly align in the longitudinal direction, while bottom cells appear more randomly oriented. Circumferential grooves induce cell alignment in the circumferential direction on both upper and lower surfaces, consistent with expectations of greater alignment on the lower surface. Longitudinal grooves also promote alignment in the longitudinal direction for both surfaces. However, their influence is minor compared to circumferential grooves. This is likely because, even without micro and nanogrooves, cells align longitudinally due to

curvature of the tubular microchannel, resulting in a minimal difference between the presence and absence of structures. The intriguing observation of a rounded distribution rather than a steep curve for longitudinal grooves on the upper surface could be attributed to the orientation angle reaching a plateau.

Comparing the orientation angle results for each tubular design (Fig. 5C), it is evident that, in all conditions, cells on the upper surface are consistently more aligned in the longitudinal direction than those on the lower surface. Furthermore, circumferential grooves have a more significant impact on cell alignment than longitudinal grooves, likely due to cells already aligning longitudinally because of the curvature. However, the fact that all circumferential grooves influence cell alignment suggests that micro- and nanogrooves have a more significant impact than curvature. These findings and the fact that circumferential grooves do not substantially affect cell migration, as seen in Fig. 3, imply that changes in cell alignment do not necessarily lead to alterations in cell migration.

Furthermore, we assessed the impact of micro- and nanogrooves on the curved surface on cell elongation, as shown in Fig. 5D. Interestingly, results for cell elongation differ from data from the orientation angle. Specifically, while circumferential grooves effectively align cells, they do not appear to promote cell migration. One might expect that cells would elongate if they were to align along the grooves in the circumferential direction; however, it seems that cells only change their direction due to the presence of micro- and nanogrooves. This phenomenon may be attributable to the limited space imposed by surrounding cells.

In contrast, longitudinal grooves generally do not differ significantly from unpatterned. Notably, only the upper surface of L0.8 exhibits enhanced cell elongation. Since all surfaces have grooves, the morphological difference in the upper and lower surfaces is not simply due to the topography. This may suggest that the differences are due to the gravity vector.[52] The results so far show that even in size ranges where curvature substantially affects cell behavior, micro- and nanogrooves have a more pronounced impact.

Discussion

In the current study, we show a tubular microchannel with a micro-/nano-topography on an inner surface to investigate the collective cell behavior affected by the curvature and topography. Researchers study the effect of curvature on cell behavior in engineered curved surfaces made of various diameters and cross-sectional shapes.[27,32] As an example, it is known that the average velocity of the collective cell migration in the tubular microchannel decreases in a diameter smaller than 100 μm due to tubular confinement.[25] Our results and a previous study[25] showed that the diameter of 100 μm is a curvature-dominant scale since the cells on the inner wall of the unpatterned tubular microchannel aligned longitudinally. Another essential factor is topography, such as micro-/nano-scale grooves, and understanding how it affects morphological guidance for the cells in the curved environment. A study utilizing a microfiber on a hemicylindrical convex (D = 250 μm) revealed that, regardless of the isotropic or anisotropic fiber, it did not alter the alignment on a cellular scale.[37] This suggests that curvature guidance dominates over microstructural contact guidance as the primary determinant of cell orientation. However, the behavior of cell sheet scale in cylindrical concave remains unexplored. Note that the convex and concave exhibit different actin filament orientations.[28,53,54] On the concave inner surface (D = 300 μm), the smooth muscle cell sheet exhibited anisotropic patterning along the micropatterned fibronectin (not engineered grooves).[41] This indicates that the topography may potentially override the curvature effects in the cell sheet scale. To contribute to this ongoing area of investigation, we developed a microchannel (D = 100 μm) with micro- and nanogrooves on its inner surface. In all designs, the layer-by-layer nature of 2PP may have introduced subtle surface features between layers; however, this effect is likely minimal due to (i) the interlayer spacing (0.3 μm) being smaller than the groove depth, and (ii) the fact that such stepping occurs uniformly across all patterns, allowing for valid comparisons of topographical effects between designs. Our model revealed that the collective cell behavior varies depending on the dimension and direction of these grooves.

Our findings show that micro-/nano-scale grooves, similar to or less than the cell size, can influence cell migration and morphology even in size ranges where curvature has a dominant effect. Regarding migration velocity V_L, the longitudinal grooves less than cell size (L4 and L0.8) enhanced V_L, while circumferential grooves did not inhibit migration. The V_L at the cell sheet edge part in unpatterned (Fig. 4D, 19.5 μm h^{-1}) is comparable to a previous report (25.2 μm h^{-1}),[25] using MDCK cells on an unpatterned microtubule (D = 100 μm). On the flat plane, cell migration velocity varies more than two-fold based on the presence and orientation of microstructures.[51] In contrast, on curved surfaces, the difference in the migration velocity in each design is not as substantial. This suggests that the topography effect is not zero but lower than the curvature in each design for collective cell migration.

In terms of the groove dimension, since the peaks of V_L and cell straightness are in both L4 and C4, the optimized dimension may exist between 800 nm and 4 μm, similar to other studies in 2D microgroove.[12,55,56] The trend similarity of cellular behavior by micro- and nanoscale grooves in 3D to 2D implies that the behavior rules may not drastically change even in a curved environment. Fluorescence staining-based orientation measurements of cells revealed an interesting phenomenon, where cells exhibited an axial orientation on the upper surface for all microstructures, distinct from the lower surface. This unique result, not reported in previous studies, may be attributed to the distinctive shape of the developed tube flow channel. Specifically, within this tube, cells enter from the flat plane at the inlet, travel along the

slope towards the lower surface, and then ascend to the upper surface, forming a cell sheet. During collective cell migration from the lower to the upper surface, it is conceivable that the lower cell group exerts a pulling force on the leading upper surface cell group, resulting in uneven forces across the cell sheet.

Curvature is known to affect cell morphology and tight junctions directly.[29] Consequently, further experiments about controlling collective epithelial rotation by cadherin knockdown cells[28] will provide insight into intercellular forces. The longitudinal orientation observed in unpatterned may result from an attempt to orient to the direction of the smaller curvature to minimize the strain.[28] Some cells are known to lift and orient perpendicular to the axis instead of deforming longitudinally to minimize displacement.[31,53] Still, the cells in our study did not show lift. Looking at the effect of microstructure on orientation, the microstructures, except L10, affected the orientation. On the other hand, the migration speed in the circumferential grooves group (C10, C4, and C0.8) has not shown obvious changes. Only from these observations may we not conclude that there is no relationship between orientation and migration velocity. If this is the case, we can assume that the circumferential groove group did not change the migration speed in this study due to the extrusion of the trailing cells or the pull from the apical region.

This study specifically investigates collective cell migration in tubular microchannels (negative curvature) with a diameter of 100 μm, limiting the curvature, groove size, and orientation. Also, exploring more complex geometries, such as zig-zag or curved microstructures, could further enhance our understanding of how cells respond to micro- and nanoscale features as shown in a previous study in 2D environment.[57] While various curved shapes, such as convex (positive curvature) cylinders and hemispheres, have been studied, there are relatively few engineered models specifically targeting concave surfaces. Furthermore, the combined effect of curvature and microstructures remains largely unknown. It is well known that curvature plays a significant role across various scales, from subcellular to supra-cellular scales (10^{-2}–10^{3} μm).[54] For diameters smaller than 100 μm (larger curvature), the influence of microstructures may be overshadowed by the effects of curvature, but further investigation is necessary to confirm this. Exploring the combination of migration velocity[58] and microstructures in tubes with diameter gradients, in addition to studying cell migration on constant diameters, is of interest. To understand the impact of geometric changes on cell morphology and behavior, advanced mathematical models that can incorporate the effects of curvature and topography are required, in addition to experimental-based approaches. This pioneering study has precisely controlled the width and direction of microstructures while investigating both dynamic and static cell behavior, revealing several intriguing phenomena. Future engineering models that can modify parameters such as the diameter, curvature, shape, and stiffness of the microchannel may further enhance our comprehension of the broader mechanisms governing cell migration.

Author contributions

Tatsuya Matsubara: writing – original draft, writing – review & editing, conceptualization, methodology, investigation, data curation, software, visualization, validation, formal analysis. Chris P. Miller: investigation, writing – review & editing. Chanhong Min: methodology, investigation, writing – review & editing, formal analysis. Chia-Yi Su: writing – review & editing. Jong Seob Choi: writing – review & editing. Chwee Teck Lim: writing – review & editing. Jude M. Phillip: methodology, writing – review & editing. Joon-wan Kim: writing – review & editing. Deok-Ho Kim: supervision, project administration, writing – review & editing, funding acquisition, conceptualization.

Conflicts of interest

The authors declare no conflict of interest.

Data availability

Supplementary information: It contains the list of 93 migration features mentioned in the *Migration feature extraction* section. See DOI: **https://doi.org/10.1039/D5LC00368G**.

All data supporting the findings of this study, including numerical values used in graphs and quantified image analysis results, are available within the article and its SI.

Acknowledgements

This work was supported by grants from the Human Frontier Science Program RGP0038/2018 (to D.-H. K.), the Uehara Memorial Foundation Postdoctoral Fellowship (to T. M.), the Japan Society for the Promotion of Science (JSPS) Overseas Research Fellowship (to T. M.), National Institutes of Health R35GM157099 (to J. M. P.), and R01CA279948 (to D.-H. K.).

References

1 S. SenGupta, C. A. Parent and J. E. Bear, *Nat. Rev. Mol. Cell Biol.*, 2021, **22**, 529–547.
2 G. C. Gurtner, S. Werner, Y. Barrandon and M. T. Longaker, *Nature*, 2008, **453**, 314–321.
3 S. Valastyan and R. A. Weinberg, *Cell*, 2011, **147**, 275–292.
4 K. Kretzschmar and F. M. Watt, *Cell*, 2012, **148**, 33–45.
5 P. Weiss and B. Garber, *Proc. Natl. Acad. Sci. U. S. A.*, 1952, **38**, 264–280.
6 C. Frantz, K. M. Stewart and V. M. Weaver, *J. Cell Sci.*, 2010, **123**, 4195–4200.
7 D. Mohammed, M. Versaevel, C. Bruyère, L. Alaimo, M. Luciano, E. Vercruysse, A. Procès and S. Gabriele, *Front. Bioeng. Biotechnol.*, 2019, **7**, 162.

8 P. Kollmannsberger, C. M. Bidan, J. W. C. Dunlop and P. Fratzl, *Soft Matter*, 2011, **7**, 9549.
9 A. Buxboim, K. Rajagopal, A. E. X. Brown and D. E. Discher, *J. Phys.: Condens. Matter*, 2010, **22**, 194116.
10 A. J. Engler, S. Sen, H. L. Sweeney and D. E. Discher, *Cell*, 2006, **126**, 677–689.
11 J. Stock and A. Pauli, *Development*, 2021, **148**, dev191767.
12 A. D. Doyle, F. W. Wang, K. Matsumoto and K. M. Yamada, *J. Cell Biol.*, 2009, **184**, 481–490.
13 C.-Y. Su, T. Matsubara, A. Wu, E. H. Ahn and D.-H. Kim, *Adv. Biol.*, 2023, 2300026.
14 P. Uttayarat, G. K. Toworfe, F. Dietrich, P. I. Lelkes and R. J. Composto, *J. Biomed. Mater. Res.*, 2005, **75A**, 668–680.
15 J. Park, D.-H. Kim, S. R. Shah, H.-N. Kim, P. Kshitiz, A. Quiñones-Hinojosa Kim and A. Levchenko, *Nat. Commun.*, 2019, **10**, 2797.
16 D. H. Kim, K. Han, K. Gupta, K. W. Kwon, K. Y. Suh and A. Levchenko, *Biomaterials*, 2009, **30**, 5433–5444.
17 D.-H. Kim, E. A. Lipke, P. Kim, R. Cheong, S. Thompson, M. Delannoy, K.-Y. Suh, L. Tung and A. Levchenko, *Proc. Natl. Acad. Sci. U. S. A.*, 2010, **107**, 565–570.
18 D.-H. Kim, C.-H. Seo, K. Han, K. W. Kwon, A. Levchenko and K.-Y. Suh, *Adv. Funct. Mater.*, 2009, **19**, 1579–1586.
19 P. Y. Mengsteab, K. Uto, A. S. T. Smith, S. Frankel, E. Fisher, Z. Nawas, J. Macadangdang, M. Ebara and D.-H. Kim, *Biomaterials*, 2016, **86**, 1–10.
20 S. Chaterji, P. Kim, S. H. Choe, J. H. Tsui, C. H. Lam, D. S. Ho, A. B. Baker and D.-H. Kim, *Tissue Eng., Part A*, 2014, **20**, 2115–2126.
21 M. Le Berre, Y.-J. Liu, J. Hu, P. Maiuri, O. Bénichou, R. Voituriez, Y. Chen and M. Piel, *Phys. Rev. Lett.*, 2013, **111**, 198101.
22 G. Charras and E. Sahai, *Nat. Rev. Mol. Cell Biol.*, 2014, **15**, 813–824.
23 B. Ladoux and R.-M. Mège, *Nat. Rev. Mol. Cell Biol.*, 2017, **18**, 743–757.
24 S. J. P. Callens, R. J. C. Uyttendaele, L. E. Fratila-Apachitei and A. A. Zadpoor, *Biomaterials*, 2020, **232**, 119739.
25 W. Xi, S. Sonam, T. B. Saw, B. Ladoux and C. T. Lim, *Nat. Commun.*, 2017, **8**, 1517.
26 F. A. Maechler, C. Allier, A. Roux and C. Tomba, *J. Cell Sci.*, 2018, jcs.222372.
27 C. M. Bidan, K. P. Kommareddy, M. Rumpler, P. Kollmannsberger, P. Fratzl and J. W. C. Dunlop, *Adv. Healthcare Mater.*, 2013, **2**, 186–194.
28 A. Glentis, C. Blanch-Mercader, L. Balasubramaniam, T. B. Saw, J. d'Alessandro, S. Janel, A. Douanier, B. Delaval, F. Lafont, C. T. Lim, D. Delacour, J. Prost, W. Xi and B. Ladoux, *Sci. Adv.*, 2022, **8**, eabn5406.
29 M. Ye, H. M. Sanchez, M. Hultz, Z. Yang, M. Bogorad, A. D. Wong and P. C. Searson, *Sci. Rep.*, 2014, **4**, 4681.
30 C. Liu, J. Xu, S. He, W. Zhang, H. Li, B. Huo and B. Ji, *J. Mech. Behav. Biomed. Mater.*, 2018, **88**, 330–339.
31 M. Werner, S. B. G. Blanquer, S. P. Haimi, G. Korus, J. W. C. Dunlop, G. N. Duda, D. W. Grijpma and A. Petersen, *Adv. Sci.*, 2017, **4**, 1600347.
32 B. Schamberger, R. Ziege, K. Anselme, M. Ben Amar, M. Bykowski, A. P. G. Castro, A. Cipitria, R. A. Coles, R. Dimova, M. Eder, S. Ehrig, L. M. Escudero, M. E. Evans, P. R. Fernandes, P. Fratzl, L. Geris, N. Gierlinger, E. Hannezo, A. Iglič, J. J. K. Kirkensgaard, P. Kollmannsberger, Ł. Kowalewska, N. A. Kurniawan, I. Papantoniou, L. Pieuchot, T. H. V. Pires, L. D. Renner, A. O. Sageman-Furnas, G. E. Schröder-Turk, A. Sengupta, V. R. Sharma, A. Tagua, C. Tomba, X. Trepat, S. L. Waters, E. F. Yeo, A. Roschger, C. M. Bidan and J. W. C. Dunlop, *Adv. Mater.*, 2023, **35**, 2206110.
33 J. A. Sanz-Herrera, P. Moreo, J. M. García-Aznar and M. Doblaré, *Biomaterials*, 2009, **30**, 6674–6686.
34 C. M. Bidan, K. P. Kommareddy, M. Rumpler, P. Kollmannsberger, Y. J. M. Bréchet, P. Fratzl and J. W. C. Dunlop, *PLoS One*, 2012, **7**, e36336.
35 S. Ehrig, B. Schamberger, C. M. Bidan, A. West, C. Jacobi, K. Lam, P. Kollmannsberger, A. Petersen, P. Tomancak, K. Kommareddy, F. D. Fischer, P. Fratzl and J. W. C. Dunlop, *Sci. Adv.*, 2019, **5**, eaav9394.
36 S. J. P. Callens, D. Fan, I. A. J. van Hengel, M. Minneboo, P. J. Díaz-Payno, M. M. Stevens, L. E. Fratila-Apachitei and A. A. Zadpoor, *Nat. Commun.*, 2023, **14**, 855.
37 M. Werner, N. A. Kurniawan, G. Korus, C. V. C. Bouten and A. Petersen, *J. R. Soc. Interface*, 2018, **15**, 20180162.
38 J. T. Elliott, A. Tona, J. T. Woodward, P. L. Jones and A. L. Plant, *Langmuir*, 2003, **19**, 1506–1514.
39 E. S. Fioretta, M. Simonet, A. I. P. M. Smits, F. P. T. Baaijens and C. V. C. Bouten, *Biomacromolecules*, 2014, **15**, 821–829.
40 K. Seunarine, M. Tormen, N. Gadegaard, M. Riehle, C. D. W. Wilkinson, L. Businaro and F. Romanato, *J. Vac. Sci. Technol., B:Microelectron. Nanometer Struct.–Process., Meas., Phenom.*, 2006, **24**, 3258.
41 Q. Jin, A. Bhatta, J. V. Pagaduan, X. Chen, H. West-Foyle, J. Liu, A. Hou, D. Berkowitz, S. C. Kuo, F. B. Askin, T. D. Nguyen, D. H. Gracias and L. H. Romer, *Sci. Adv.*, 2020, **6**, eaaz2598.
42 P. Zorlutuna, P. Vadgama and V. Hasirci, *J. Tissue Eng. Regener. Med.*, 2010, **4**, 628–637.
43 N. Gadegaard, M. J. Dalby, M. O. Riehle, A. S. G. Curtis and S. Affrossman, *Adv. Mater.*, 2004, **16**, 1857–1860.
44 M. Thiel and M. Hermatschweiler, *Opt. Photonik*, 2011, **6**, 36–39.
45 M. Mao, J. He, X. Li, B. Zhang, Q. Lei, Y. Liu and D. Li, *Micromachines*, 2017, **8**, 113.
46 S. Kawata, H.-B. Sun, T. Tanaka and K. Takada, *Nature*, 2001, **412**, 697–698.
47 A. Sharaf, J.-P. Frimat and A. Accardo, *Mater. Today Bio*, 2024, **29**, 101325.
48 D. Maity, N. Sivakumar, P. Kamat, N. Zamponi, C. Min, W. Du, H. Jayatilaka, A. Johnston, B. Starich, A. Agrawal, D. Riley, L. Venturutti, A. Melnick, L. Cerchietti, J. Walston and J. M. Phillip, *Adv. Sci.*, 2024, **11**, 2400918.
49 J. M. Phillip, N. Zamponi, M. P. Phillip, J. Daya, S. McGovern, W. Williams, K. Tschudi, H. Jayatilaka, P.-H. Wu, J. Walston and D. Wirtz, *Commun. Biol.*, 2021, **4**, 1–9.
50 D. Maity, N. Sivakumar, P. Kamat, N. Zamponi, C. Min, W. Du, H. Jayatilaka, A. Johnston, B. Starich, A. Agrawal, D.

Riley, L. Venturutti, A. Melnick, L. Cerchietti, J. Walston and J. M. Phillip, *Adv. Sci.*, 2024, **11**, 2400918.
51 H. N. Kim, Y. Hong, M. S. Kim, S. M. Kim and K.-Y. Suh, *Biomaterials*, 2012, **33**, 8782–8792.
52 S. Sakakibara, S. A. Abdellatef, S. Yamamoto, M. Kamimura and J. Nakanishi, *Sci. Technol. Adv. Mater.*, 2023, **24**, 2206525.
53 M. Werner, A. Petersen, N. A. Kurniawan and C. V. C. Bouten, *Adv. Biosyst.*, 2019, **3**, 1900080.
54 S.-M. Yu, J. M. Oh, J. Lee, W. Lee-Kwon, W. Jung, F. Amblard, S. Granick and Y.-K. Cho, *Acta Biomater.*, 2018, **77**, 311–321.
55 K. A. Diehl, J. D. Foley, P. F. Nealey and C. J. Murphy, *J. Biomed. Mater. Res.*, 2005, **75A**, 603–611.
56 V. Raghunathan, C. McKee, W. Cheung, R. Naik, P. F. Nealey, P. Russell and C. J. Murphy, *Tissue Eng., Part A*, 2013, **19**, 1713–1722.
57 K. W. Kwon, H. Park and J. Doh, *PLoS One*, 2013, **8**, e73960.
58 M. Sentoku, K. Iida, H. Hashimoto and K. Yasuda, *Biophys. Rep.*, 2022, **2**, 100063.
59 T. Matsubara, J.S. Choi, D.-H. Kim and J.-W. Kim, *Small*, 2022, **18**(15), e2106221.
60 T. Matsubara, H.H. Huynh, K. Yoshida and J.-W. Kim, *Sens. Actuators, A*, 2019, **295**, 317–323.
61 J.S. Choi, A.S.T. Smith, N.P. Williams, T. Matsubara, M. Choi, J.-W. Kim, H.J. Kim, S. Choi and D.-H. Kim, *Adv. Funct. Mater.*, 2020, **30**(25), 33244297.
62 T. Otomo, H. Noh, T. Matsubara, D.-H. Kim, M. Ikeuchi, K. Yoshida and J.-W. Kim, *Biochip J*, 2025, **19**(1), 91–98.
63 T. Otomo, T. Matsubara, K. Yoshida, D.-H. Kim, M. Ikeuchi and J.-W. Kim, *Sens. Actuators, A*, 2023, **356**, 114332.